



CrossMark
click for updates

Cite this: *Nanoscale*, 2016, 8, 20118

Direction-resolved radiation from polarization-controlled surface plasmon modes on silver nanowire antennas†

Zhili Jia,^a Hong Wei,^{*a} Deng Pan^b and Hongxing Xu^{b,c}

Metallic nanowires (NWs) support multiple surface plasmon (SP) modes, which lead to extraordinary SP propagation behaviors. The leaky SP modes in metallic NWs connect the guiding and radiation of light at the nanometer scale. Understanding and controlling these modes are of vital importance for various nanophotonic applications. Here, we investigate the radiation from two polarization-controlled SP modes on supported silver NWs by using leakage radiation imaging and Fourier imaging techniques. The radiation directions from these modes can be clearly resolved from the Fourier images. The radiation polarization of the SP modes is related to the polarization of the excitation light. By depositing thin Al₂O₃ films onto silver NWs or decreasing the excitation wavelength, the radiation angles and wave vectors of the two modes are increased, and the longitudinal mode is more sensitive to Al₂O₃ thickness. Moreover, the propagation length of the longitudinal mode is obtained by analyzing the leakage radiation images, which is decreased with the decrease of the excitation wavelength and the increase of the Al₂O₃ layer thickness. These results show that leakage radiation from different SP modes on silver NWs can be resolved directly and controlled effectively. The supported silver NWs can thus be applied to designing plasmonic circuits, nanoantennas and nanosensors.

Received 13th September 2016,
Accepted 11th November 2016

DOI: 10.1039/c6nr07242a

www.rsc.org/nanoscale

Introduction

Benefiting from the subwavelength confinement feature of surface plasmons (SPs), surface waves of collective oscillations of free electrons at the metal–dielectric interface, plasmonic waveguides can perform the function of optical fibers at the deep subwavelength scale and construct plasmonic devices to integrate with nanoelectronic devices for high speed nanophotonic circuitry.^{1–3} Chemically synthesized silver nanowires (Ag NWs) with crystalline structures are efficient plasmonic waveguides due to their low SP propagation losses.^{4–9} Silver NWs have also been used for building hybrid plasmonic–photonic devices,^{10–12} investigating coupling with quantum emitters,^{13–19} and constructing nanowire networks.^{20–22} The Ag NWs can support multiple SP modes, which are the physical origins of various optical phenomena in the NWs.^{23–25} The SP modes can be tuned by the polarization of the excitation light,²⁶ the dielectric environment²⁷ and the structural-

asymmetry-induced mode conversion.²⁸ By controlling the components of the SP modes, peculiar SP properties can be obtained, such as tunable emission polarization²⁹ and chiral propagation.³⁰ The excitation of multiple SP modes enables the manipulation of light transmission in Ag NW networks, which has been used to realize plasmonic devices, such as routers,^{24,31} wavelength splitters,^{27,31,32} modulators³³ and logic gates.^{26,34} Recently, collimated SP beams originating from the interference between film-SPs generated by two NW SP modes have been investigated in the Ag NW/Al₂O₃/Ag film composite structure.³⁵ Thus, the SP modes play an important role in controlling the SP propagation and determining the performances of NW-based plasmonic devices.

The SP modes in substrate-supported Ag NWs can be leaky modes with effective refractive indices smaller than that of the substrate. From the side of the transparent substrate, like glass, leaky radiation can be detected. The technique of real space imaging together with Fourier imaging based on this leaky radiation is usually called leakage radiation microscopy (LRM), which has been used for studies of propagating SPs. By this technique, both the real space image and Fourier image can be obtained and quantitatively analyzed. From the real space image, a spatial SP field profile and propagation length can be obtained, while from the Fourier image, the leakage radiation angle, wave vector, and effective refractive index can

^aBeijing National Laboratory for Condensed Matter Physics, Institute of Physics, Chinese Academy of Sciences, Beijing 100190, China. E-mail: weihong@iphy.ac.cn

^bSchool of Physics and Technology, Wuhan University, Wuhan 430072, China

^cInstitute for Advanced Studies, Wuhan University, Wuhan 430072, China

†Electronic supplementary information (ESI) available. See DOI: 10.1039/c6nr07242a

be extracted.^{36,37} The LRM studies reveal that substrate-supported Ag NWs can work as broadband unidirectional antennas to radiate in well-defined directions.^{38–40} In spite of these research studies on SPs in Ag NWs by LRM, there is a rare experimental study for different leaky plasmon modes on NWs using this technique.⁴¹

In this work, we investigate the radiation from different modes of SPs on supported Ag NWs by using leakage radiation imaging and Fourier imaging methods. By controlling the polarization of the excitation light, two leaky SP modes can be selectively excited. The radiation from these two modes is direction-resolved, as demonstrated by Fourier images. The simultaneous excitation of both modes results in zigzag intensity distribution in the leakage radiation image, resulting from the coherent superposition of the two modes. The analysis of the polarization of the leakage radiation shows that the emission along the axis of the NW maintains the polarization of the excitation light. The radiation angles from the two modes can be well controlled by coating the Al₂O₃ film on the Ag NW. By exciting the SPs using lasers of different wavelengths, dispersion relations are obtained. Depositing Al₂O₃ films on the Ag NWs increases the wave vectors of the SP modes, and the longitudinal mode is more sensitively dependent on the Al₂O₃ layer thickness. The propagation length of the longitudinal mode is also investigated, which decreases with the decrease of the excitation wavelength and the increase of the Al₂O₃ layer thickness.

Methods

Schematic illustration of the Fourier imaging setup and the definition of azimuthal angles (θ and φ) can be found in the references.^{38,40} Fig. 1 shows a simple sketch for the leaky radiation of SPs along the direction parallel to the axis of a Ag NW ($\varphi = 0$). The wave vector of the SP leaky mode is smaller than the wave vector of the photon in the glass substrate. Therefore, the leaky mode radiates into the substrate with the angle θ determined by the phase matching condition. The relationship between the two wave vectors for $\varphi = 0$ is described by the following equation:

$$\text{Re}(k_{\text{SP}}) = k_{\text{photon}} \sin \theta \quad (1)$$

where $\text{Re}(k_{\text{SP}})$ is the wave vector of the SPs on the Ag NW along the NW axis, $k_{\text{photon}} = 2n_{\text{glass}}\pi/\lambda$ is the wave vector of photons in the glass substrate, and θ is the angle between the leakage radiation direction and the direction perpendicular to the

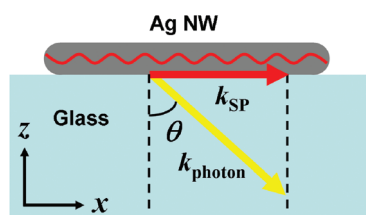


Fig. 1 Schematic illustration of the relation between the two wave vectors $\text{Re}(k_{\text{SP}})$ and k_{photon} .

plane of the glass substrate. In the experiments, the Ag NWs synthesized by the chemical method are put on a cleaned cover glass substrate. From the other side of the glass, one end of the Ag NW is illuminated by focused laser beams with different wavelengths λ (532, 633, and 785 nm) to generate propagating SPs. Here, a high numerical aperture (NA) oil immersion objective (magnification 100 \times , NA = 1.49) is used to focus the laser light and collect the radiation signals from the supported Ag NWs. According to the numerical aperture equation $\text{NA} = n \sin \theta$, the maximum collection angle of the oil immersion objective is determined to be about 78.98 $^\circ$. Here $n = 1.518$ is the refractive index of the index-matching oil.

The numerical mode analyses based on the finite element method (FEM) are applied to calculate the electric field distributions, the charge distributions, and the dispersion relations of the leaky SP modes. In simulation, the cross section of the NW is modeled as a pentagon and the corners are blunted with a radius of 5 nm. The effective refractive indices of the glass substrate and the Al₂O₃ are 1.518 and 1.765,⁴² respectively. The dielectric constant of silver is from the interpolated experimental data.⁴³ The perfectly matched layer enclosing the simulation region is applied to absorb the leakage radiation from the SP modes. By performing the mode analyses, both the field distributions and the effective refractive indices n_{eff} of the two SP modes for a certain wavelength λ are obtained. Then the real part of the wave vector $\text{Re}(k_{\text{SP}}) = 2\pi \text{Re}(n_{\text{eff}})/\lambda$ is obtained. By sweeping the wavelength in the simulation and calculating the corresponding $\text{Re}(k_{\text{SP}})$, we can obtain the dispersion relation of the mode and compare it with the experimental result.

Results and discussion

Resolving the directions and polarizations of radiation from different SP modes

The scanning electron microscopy (SEM) image for a Ag NW with a radius of 180 nm and a length of 27.1 μm is shown in Fig. 2a. The top end of the Ag NW is illuminated by a laser light of 532 nm wavelength. Leakage radiation can be observed as the propagating SPs radiate into the substrate, as shown in the top panels of Fig. 2b. An aperture is used to select certain areas of the Ag NW for Fourier imaging. The bottom panels in Fig. 2b show the Fourier images corresponding to the area outlined by the dashed rectangle in Fig. 2bi. The data in Fig. 2bi and ii correspond to the laser polarization parallel and perpendicular to the Ag NW, respectively. We call the two corresponding SP modes excited under these two polarizations the longitudinal mode and the transverse mode. When the polarization of incident light is parallel to the Ag NW, the longitudinal mode is excited and the leakage radiation is symmetrically distributed on the two sides of the NW. In the corresponding Fourier image, a straight bright line with a minimum intensity at $\varphi = 0$ is shown. When the polarization of the incident light is perpendicular to the Ag NW, the transverse mode is excited and the distribution of leakage radiation is also symmetrical. In the corresponding Fourier image, a straight line with a

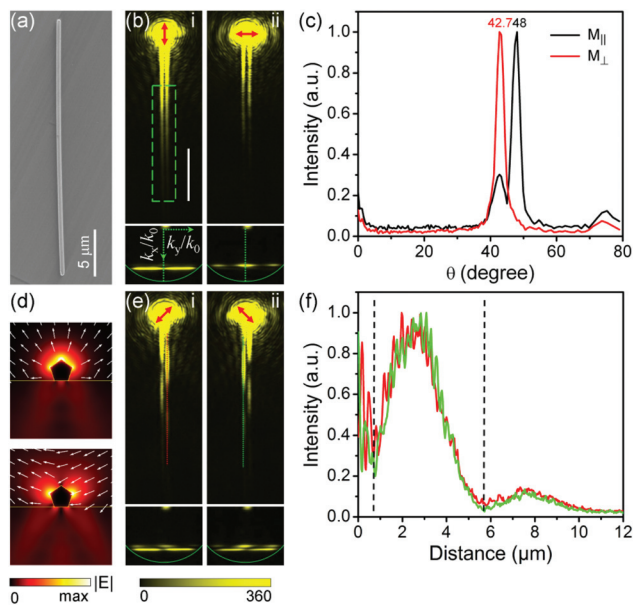


Fig. 2 Resolving the directions of radiation from different modes. (a) SEM image of a Ag NW with a radius of 180 nm and a length of 27.1 μm . (b, e) The leakage radiation images (top) and corresponding Fourier images (bottom) detected from the glass side. The red arrows indicate the polarization directions of the incident laser light with a 532 nm wavelength. Fourier images are obtained from the area marked by a green dashed rectangle in (bi). The green circles in the Fourier images represent the maximum radiation angle that can be collected by the experimental system. k_x/k_0 and k_y/k_0 in (bi) denote the wave vectors of the SP modes normalized by the wave vector of light in vacuum. The laser power is 0.02 μW . The exposure time of leakage radiation and Fourier images is 100 ms unless specified. The color bar applies to all leakage radiation and Fourier images unless specified. The scale bar in (bi) is 5 μm . (c) The intensity versus θ along the direction $\varphi = 0$ as marked by the green dashed lines in the Fourier images. $M_{||}$ and M_{\perp} indicate the longitudinal mode and the transverse mode, respectively. (d) The calculated electric field distributions of the longitudinal mode (top) and transverse mode (bottom) of SPs on a glass-supported Ag NW without Al_2O_3 layers. The NW radius is 170 nm. The wavelength is 532 nm. (f) The intensity distributions along the red and green dashed lines in (e). The two black dashed lines mark one period of the zigzag pattern.

maximum intensity at $\varphi = 0$ is observed. The pattern of the Fourier image for a certain SP mode reflects the far field electric field distribution of the radiation detected by the experimental setup.

Eqn (1) can be rewritten as $\text{Re}(k_{\text{SP}})/k_0 = n_{\text{glass}} \sin \theta$, where $k_0 = 2\pi/\lambda$ is the wave vector of light in vacuum. The real part of the effective refractive index $\text{Re}(n_{\text{eff}}) = \text{Re}(k_{\text{SP}})/k_0$ of the leaky SP modes can be obtained directly from the Fourier images, as illustrated by k_x/k_0 in Fig. 2bi. Then the wave vector and the radiation angle θ of the SPs can be extracted. From Fig. 2b, the effective refractive indices of the two modes are determined to be 1.1285 and 1.0299, respectively. Fig. 2c shows the intensity distributions versus θ along the direction $\varphi = 0$ as marked by green dashed lines in the Fourier images in Fig. 2bi and ii. The radiation angles from the longitudinal mode and transverse mode are 48° and 42.7° , respectively. Full width at half maximum (FWHM) of the two peaks is as narrow as 3° . This

indicates that the radiation from the two modes has high directivity and the supported Ag NW can serve as a highly directional nanoantenna with two radiation modes. It is noted that the experimentally measured FWHM is limited by the aperture used for selecting the area for Fourier imaging due to the diffraction of light, and the real FWHM of the radiation from the NW antenna can be narrower.

Fig. 2d shows the simulated electric field distributions of the two modes obtained by FEM using the perfectly matched layer boundary condition. For the longitudinal mode, the field is mainly localized at the top of the Ag NW, whereas the field of the transverse mode is mainly localized at the two sides of the Ag NW. The electric field radiated into the glass also shows different distributions for the two modes. For the longitudinal mode, more energy is radiated to the two sides, whereas for the transverse mode, energy is radiated to the two sides and the center. This agrees well with the patterns in corresponding Fourier images measured in the experiment. The patterns of the far field radiation depend on the charge distributions of the SP modes on the NW. For a metallic NW deposited on a substrate, the charge distributions of the SP modes are changed compared to that for a NW without substrate due to the substrate-induced hybridization of SP modes.⁴⁴ The charge distributions of the two modes we studied have the feature of quadrupole mode, as shown in ESI Fig. S1.† For the longitudinal mode, the charges near the substrate form two opposite dipoles and thus radiate into two sides. For the transverse mode, the charges on the horizontal edge at the bottom and the adjacent edges form three dipoles which lead to the three lobes in the radiation pattern.

The Ag NW in Fig. 2a is also illuminated by the laser light of other polarizations to excite both modes. Fig. 2ei and ii show the leakage radiation images and the corresponding Fourier images for the polarization angles of 45° and -45° with respect to the axis of the Ag NW. It can be clearly seen that the leakage radiation shows zigzag distributions along the Ag NW, which originate from the coherent superposition of the two modes. From the Fourier images, two obviously distinguishable straight lines with different intensity variation patterns are observed, corresponding to the radiation from the two modes. Fig. 2f shows the intensity profiles along the red and green dashed lines in Fig. 2ei and ii, from which the period of the zigzag pattern is determined to be about 5.1 μm . The period Λ of the zigzag distribution of leakage radiation on the Ag NW is related to the real part of effective refractive index of SPs by the following equation:²⁷

$$\Lambda = \frac{\lambda}{\text{Re}(n_{\text{eff}||}) - \text{Re}(n_{\text{eff}\perp})} \quad (2)$$

where $\text{Re}(n_{\text{eff}||})$ and $\text{Re}(n_{\text{eff}\perp})$ are the real parts of effective refractive indices of the longitudinal mode and transverse mode, respectively. Using the effective refractive indices of the two modes obtained from the Fourier images, the period calculated from eqn (2) is 5.4 μm , which agrees well with the value obtained directly from the leaky radiation images.

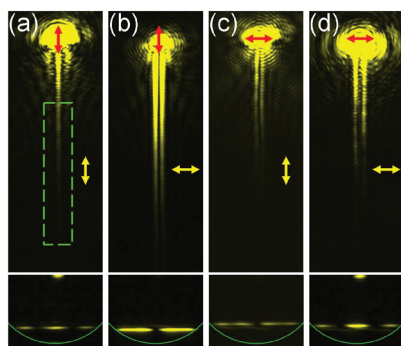


Fig. 3 The emission polarization characteristics of leakage radiation from longitudinal (a, b) and transverse (c, d) modes. Top and bottom panels are the leakage radiation images and corresponding Fourier images, respectively. The red arrows indicate the polarizations of the excitation light with a 532 nm wavelength. The yellow arrows indicate the emission polarizations. Fourier images are obtained from the area marked by a green dashed rectangle in (a). The exposure time of the Fourier image in (c) is 300 ms, and for all the other images is 200 ms. The intensity range for the color scale of the images in (c) is 0–180, and for others is 0–360.

The emission polarization characteristics of the leakage radiation from these two modes on the Ag NW in Fig. 2b are further investigated by using a polarizer to analyze the emission polarization, as shown in Fig. 3. The leakage radiation images show different intensity distributions depending on the excitation polarization and the radiation polarization, revealing the spatial variation of the polarization components for the two leaky modes (see ESI Fig. S2†). The Fourier images show that the polarizations of the leakage radiation from the two modes are dependent on the radiation directions. For the longitudinal mode, when the polarizing axis of the polarizer is parallel to the Ag NW (Fig. 3a), the leakage radiation is mainly concentrated along $\varphi = 0$ and the intensity on the two sides is weak. When the polarizing axis is perpendicular to the Ag NW (Fig. 3b), the intensity distribution in the Fourier image splits into two parts and the intensity along $\varphi = 0$ is 0. For the transverse mode, when the polarizing axis is parallel to the NW (Fig. 3c), the Fourier image pattern is similar to that in Fig. 3b. When the polarizing axis is perpendicular to the NW (Fig. 3d), the intensity distribution in the Fourier image splits to three parts, similar to the Fourier pattern in Fig. 3a. From these polarization dependent Fourier images, we can see that the polarization of the SP radiation along $\varphi = 0$ is parallel to the Ag NW in the image plane for the longitudinal mode, while perpendicular to the NW for the transverse mode. These results show that the polarizations of the SP radiation along $\varphi = 0$ maintain the polarizations of incident light. The images for more polarization directions of the analyzer are shown in ESI Fig. S3.†

The polarization-maintaining properties of the SP radiation along $\varphi = 0$ can be understood from the symmetry of the structure. Since the Ag NW on the substrate is mirror symmetric with respect to the vertical plane across the central axis of the NW, the symmetry of the electric field distribution accords with the symmetry of the excitation polarization (symmetric and anti-

symmetric for parallel and perpendicular polarization, respectively), which implies that the polarization of the electric field on every point on the mirror plane remains the same as the excitation polarization. This phenomenon can also be straightforwardly understood from the charge distributions in ESI Fig. S1.† For the longitudinal mode, the interference of the radiation from the two dipoles at the bottom edge cancels the in-plane field component, leaving a net electric field along the NW. For the transverse mode, the radiation along the NW is directly from the horizontal dipole at the bottom edge, and therefore the polarization of the radiation is perpendicular to the NW.

Controlling the leakage radiation by depositing Al_2O_3 films

The change of the surrounding environment induces the change of the wave vectors of SPs.^{27,40} Thus the leakage radiation angles from different modes on the Ag NW can be tuned by depositing an Al_2O_3 film of different thicknesses. We investigate another Ag NW with a radius of about 170 nm coated with a layer of Al_2O_3 with different thicknesses. The deposition of the Al_2O_3 layer is achieved by using the atomic layer deposition (ALD) technique. The increment step of the Al_2O_3 layer thickness is 10 nm. Fig. 4 shows the dependence of radiation on the Al_2O_3 thickness for longitudinal and transverse modes excited by laser light of 532 nm wavelength (see ESI Fig. S4† for radiation of transverse mode with Al_2O_3 layer of 30 nm

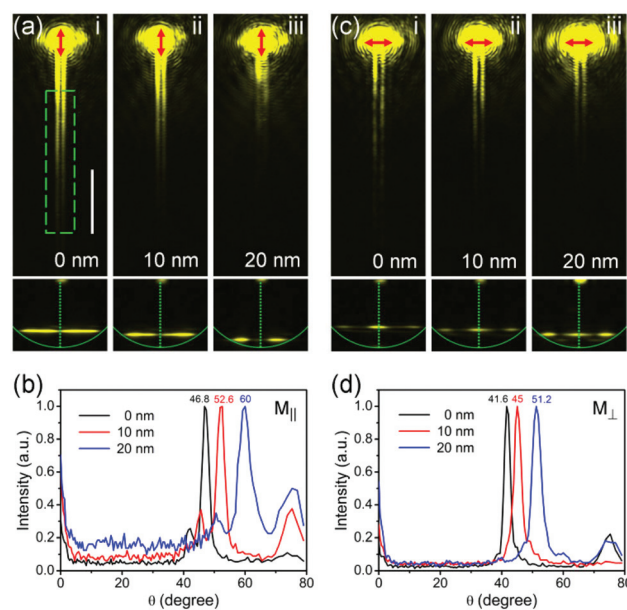


Fig. 4 The radiation from longitudinal and transverse modes for different Al_2O_3 thicknesses. (a, c) Leakage radiation images (top) and corresponding Fourier images (bottom) for different thicknesses of the Al_2O_3 layer. The red arrows indicate the polarization directions of the laser light with a 532 nm wavelength. Fourier images are obtained from the area marked by a green dashed rectangle in (ai). The exposure time of the Fourier image in (ciii) is 300 ms, and for others is 100 ms. The scale bar in (ai) is 5 μm . (b, d) The analysis of radiation angles for longitudinal (b) and transverse (d) modes along the direction $\varphi = 0$ as marked by green dashed lines in (a) and (c).

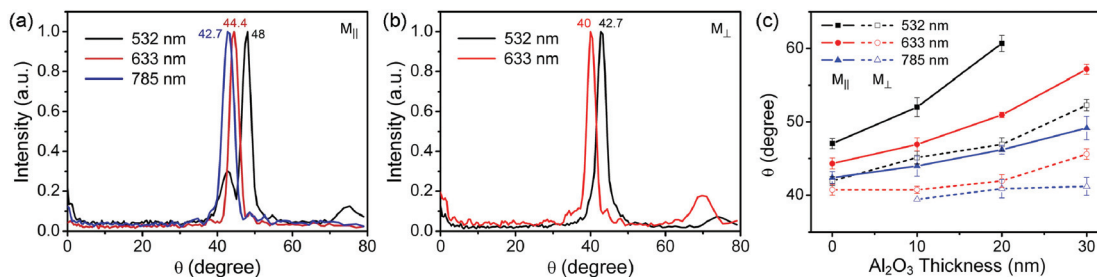


Fig. 5 (a, b) The radiation angles for longitudinal (a) and transverse (b) modes under different laser wavelengths (532, 633, and 785 nm). The curves show the intensity versus θ along the direction $\varphi = 0$. (c) The radiation angles of two modes as a function of Al_2O_3 layer thickness for excitation wavelengths of 532, 633, and 785 nm. The solid symbols and hollow symbols are experimental means of five NWs for longitudinal mode and transverse mode, respectively. The error bars show the standard deviation. The lines are used as guide to the eye.

thickness). From the leakage radiation images, we can see that the radiation from both modes becomes weaker with the increase of the Al_2O_3 layer thickness, especially for the longitudinal mode. Meanwhile the radiation angle becomes larger as can be seen from the corresponding Fourier images. Moreover, the intensity distributions along the horizontal bright lines of the Fourier imaging patterns also change. As can be seen, with the increase of the Al_2O_3 layer thickness, the bright line in the Fourier image is separated into two parts gradually for the longitudinal mode. The electric field distributions of the two modes for Ag NWs coated with an Al_2O_3 layer of 20 nm thickness are also calculated as shown in ESI Fig. S5.† The simulation results show that, by depositing an Al_2O_3 layer of 20 nm thickness, the electric field distribution radiated into the glass changes, which agrees with the experimental Fourier imaging results in Fig. 4a and c.

The radiation angles of longitudinal and transverse modes along $\varphi = 0$ direction for different thicknesses of the Al_2O_3 layer are shown in Fig. 4b and d, respectively. By increasing the Al_2O_3 thickness from 0 nm to 10 nm (the first 10 nm), the increase of the radiation angle for the longitudinal and transverse modes is 0.58° and 0.34° , respectively, by depositing 1 nm Al_2O_3 in average. For the second 10 nm, the average increase is 0.74° and 0.62° per nm Al_2O_3 , respectively. For the third 10 nm, the average increase for transverse mode is 1.05° . These analyses indicate that the radiation angles from both modes can be largely changed by depositing Al_2O_3 layers on the Ag NW, and the longitudinal mode is more sensitive to the Al_2O_3 thickness change. With the increase of the Al_2O_3 thickness, the increasing rate of the radiation angle for both modes becomes larger. It is noted that besides Al_2O_3 , other transparent materials with a high refractive index can also be used for the coating film to change the wave vectors of the SP modes, and thus to change the radiation angles. By dynamically tuning the refractive index of specific coating material, the SP radiation can be dynamically modulated.

Leakage radiation for different wavelengths

We further investigate the leakage radiation dependence on the excitation wavelength. Three lasers of different wavelengths (532, 633, and 785 nm) are used to excite the Ag NW in Fig. 2a. The radiation angles for longitudinal and transverse modes

are analyzed and shown in Fig. 5a and b (see ESI Fig. S6† for the leakage radiation images and corresponding Fourier images). When the wavelength of the incident light is increased, the radiation angles of both longitudinal and transverse modes are decreased. For the longitudinal mode, the radiation angle shifts about 3.6° when the wavelength changes from 532 nm to 633 nm. The corresponding shift for the transverse mode is about 2.7° .

We analyze the radiation angles of longitudinal and transverse modes for five Ag NWs with variable thicknesses of the Al_2O_3 layer. These five Ag NWs have similar radii ranging from 160 nm to 183 nm. Fig. 5c shows the radiation angles of the two modes as a function of the Al_2O_3 thickness for different excitation wavelengths. It is found that the radiation angles of the two modes increase faster with the decrease of the excitation wavelength and the increase of the Al_2O_3 layer thickness.

The change of the radiation angle originates from the change of the SP wave vector. In order to get the dispersion relations of the leaky SP modes on supported Ag NWs, we calculate the wave vectors of SPs for the five Ag NWs used in Fig. 5c. Fig. 6a and b show the dispersion relations of the two modes for different Al_2O_3 thicknesses. The simulation results agree well with the experimental data. The changing of wave vectors for both modes shows the same trends of dependence on the photon energy and Al_2O_3 thickness as the radiation angles. The increasing of wave vectors with the increase of the Al_2O_3 thickness is more remarkable for the larger photon energy. Moreover, the wave vector of the longitudinal mode is changed more sensitively compared to the transverse mode with the increase of the Al_2O_3 thickness (see ESI Fig. S7†).

Propagation lengths of SPs for different wavelengths and different Al_2O_3 thicknesses

The propagation lengths of the two modes can be analyzed from the corresponding leakage radiation images. Fig. 7b shows the leakage radiation intensity along the red and green dashed lines in Fig. 7ai and ii. The propagation lengths of the two modes can be obtained directly by fitting each curve to an exponential decay function:

$$I(x) = I_0 e^{-x/L_{\text{SP}}} \quad (3)$$

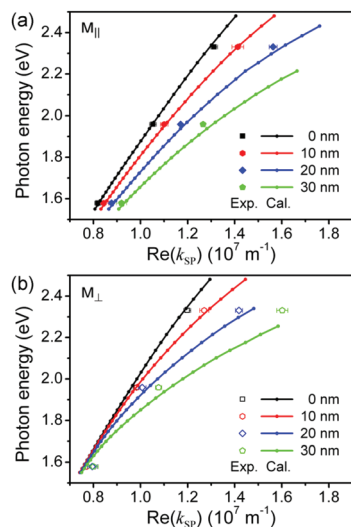


Fig. 6 The dispersion relations of longitudinal mode (a) and transverse mode (b) of SPs on glass-supported Ag NWs for Al₂O₃ thicknesses of 0, 10, 20, and 30 nm. The experimental data are mean values of five NWs and the error bars show the standard deviation. The lines are calculated data for Ag NWs of a radius of 170 nm.

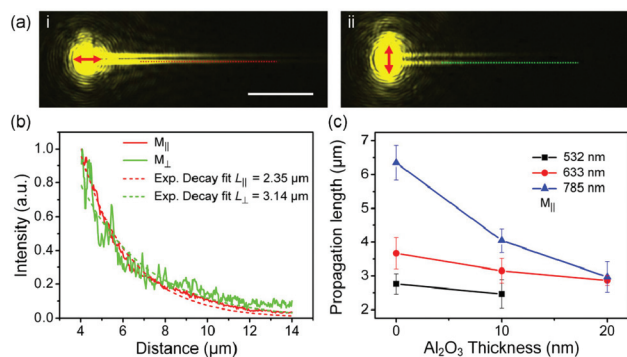


Fig. 7 The propagation lengths of SPs for different excitation wavelengths and different Al₂O₃ thicknesses. (a) The leakage radiation images for longitudinal mode (i) and transverse mode (ii), respectively. The scale bar in (ai) is 5 μm. (b) The analysis of the propagation lengths of two modes. The two curves show intensity distributions along the red and green dashed lines in (ai) and (aii). $L_{||}$ and L_{\perp} indicate the propagation lengths of longitudinal mode and transverse mode, respectively. (c) The propagation lengths of the longitudinal mode for different excitation wavelengths and different Al₂O₃ thicknesses. The experimental data (solid symbols) are mean values from five NWs and the error bars show the standard deviation. The solid lines are used as guide to the eye.

where I_0 is the initial intensity of the SPs at the starting point and L_{SP} is the propagation length of SPs decaying to $1/e$ of the original intensity. By fitting the curves in Fig. 7b, we obtain the propagation lengths for longitudinal and transverse modes are 2.35 μm and 3.14 μm, respectively, for an excitation wavelength of 532 nm.

We analyze the propagation lengths of the longitudinal mode for the five NWs investigated in Fig. 6 and the results are shown in Fig. 7c. With the increase of the excitation wave-

length, the propagation length increases. With the increase of the Al₂O₃ layer thickness, the propagation length decreases markedly, especially for the longer wavelength. For a shorter wavelength and a thicker Al₂O₃ film, the SPs are more tightly confined on the NW with more energy in silver (see ESI Fig. S8[†]), leading to larger Ohmic losses, so that the propagation length is decreased.

Conclusion

The radiation from different modes of SPs on supported Ag NWs is investigated by using leakage radiation imaging and Fourier imaging. We demonstrate that the radiation directions of two modes can be resolved facilely in the Fourier images. The radiation along the central axis of the NW maintains the polarization of the excitation light, indicating the different polarization characteristics of the two modes. The radiation can be readily controlled by depositing Al₂O₃ films of different thicknesses on the Ag NWs and using different excitation wavelengths. With the increase of the Al₂O₃ layer thickness and the decrease of the excitation wavelength, the radiation angles of the two modes increase and the increasing rate becomes larger. By analyzing the dispersion relations, it is found that the radiation angle and the wave vector of the longitudinal mode are more sensitively dependent on the Al₂O₃ thickness. It is also found that the propagation length decreases with the increase of the Al₂O₃ layer thickness and the decreasing rate is higher for the longer wavelength. Our results reveal the leakage radiation properties of different SP modes and show how they can be controlled by tuning polarization, dielectric coating and excitation wavelengths. These findings are important for exploiting SP leaky modes for subwavelength light guiding and directional radiation, which will be helpful for designing plasmonic circuits, nanoantennas and sensors.

Acknowledgements

This work was supported by the Ministry of Science and Technology of China (Grant No. 2015CB932400), the National Natural Science Foundation of China (Grant No. 11422436, 11374012, 11227407 and 11134013), the Prominent Young Scientist Program and the Strategic Priority Research Program (B) (Grant No. XDB07030100) of the Chinese Academy of Sciences (CAS), and New Star of the Science and Technology Program of Beijing Municipal Science and Technology Commission. We thank the Laboratory of Microfabrication in the Institute of Physics, CAS for experimental support.

References

- 1 E. Ozbay, *Science*, 2006, **311**, 189–193.
- 2 D. K. Gramotnev and S. I. Bozhevolnyi, *Nat. Photonics*, 2010, **4**, 83–91.

- 3 H. Wei and H. X. Xu, *Nanophotonics*, 2012, **1**, 155–169.
- 4 H. Ditlbacher, A. Hohenau, D. Wagner, U. Kreibitz, M. Rogers, F. Hofer, F. R. Aussenegg and J. R. Krenn, *Phys. Rev. Lett.*, 2005, **95**, 257403.
- 5 A. W. Sanders, D. A. Routenberg, B. J. Wiley, Y. N. Xia, E. R. Dufresne and M. A. Reed, *Nano Lett.*, 2006, **6**, 1822–1826.
- 6 M. Allione, V. V. Temnov, Y. Fedutik, U. Woggon and M. V. Artemyev, *Nano Lett.*, 2008, **8**, 31–35.
- 7 C. Rewitz, T. Keitzl, P. Tuchscherer, J. S. Huang, P. Geisler, G. Razinskas, B. Hecht and T. Brixner, *Nano Lett.*, 2012, **12**, 45–49.
- 8 X. Guo, Y. G. Ma, Y. P. Wang and L. M. Tong, *Laser Photonics Rev.*, 2013, **7**, 855–881.
- 9 X. Xiong, C. L. Zou, X. F. Ren, A. P. Liu, Y. X. Ye, F. W. Sun and G. C. Guo, *Laser Photonics Rev.*, 2013, **7**, 901–919.
- 10 X. Guo, M. Qiu, J. M. Bao, B. J. Wiley, Q. Yang, X. N. Zhang, Y. G. Ma, H. K. Yu and L. M. Tong, *Nano Lett.*, 2009, **9**, 4515–4519.
- 11 X. Q. Wu, Y. Xiao, C. Meng, X. N. Zhang, S. L. Yu, Y. P. Wang, C. X. Yang, X. Guo, C. Z. Ning and L. M. Tong, *Nano Lett.*, 2013, **13**, 5654–5659.
- 12 M. Li, C. L. Zou, X. F. Ren, X. Xiong, Y. J. Cai, G. P. Guo, L. M. Tong and G. C. Guo, *Nano Lett.*, 2015, **15**, 2380–2384.
- 13 Y. Fedutik, V. V. Temnov, O. Schops, U. Woggon and M. V. Artemyev, *Phys. Rev. Lett.*, 2007, **99**, 136802.
- 14 A. V. Akimov, A. Mukherjee, C. L. Yu, D. E. Chang, A. S. Zibrov, P. R. Hemmer, H. Park and M. D. Lukin, *Nature*, 2007, **450**, 402–406.
- 15 R. Kolesov, B. Grotz, G. Balasubramanian, R. J. Stohr, A. A. L. Nicolet, P. R. Hemmer, F. Jelezko and J. Wrachtrup, *Nat. Phys.*, 2009, **5**, 470–474.
- 16 H. Wei, D. Ratchford, X. Q. Li, H. X. Xu and C. K. Shih, *Nano Lett.*, 2009, **9**, 4168–4171.
- 17 S. Kumar, N. I. Kristiansen, A. Huck and U. L. Andersen, *Nano Lett.*, 2014, **14**, 663–669.
- 18 Q. Li, H. Wei and H. X. Xu, *Nano Lett.*, 2014, **14**, 3358–3363.
- 19 Q. Li, H. Wei and H. X. Xu, *Nano Lett.*, 2015, **15**, 8181–8187.
- 20 E. C. Garnett, W. S. Cai, J. J. Cha, F. Mahmood, S. T. Connor, M. G. Christoforo, Y. Cui, M. D. McGehee and M. L. Brongersma, *Nat. Mater.*, 2012, **11**, 241–249.
- 21 S. W. Dai, Q. Li, G. P. Liu, H. B. Yang, Y. Q. Yang, D. Zhao, W. Wang and M. Qiu, *Appl. Phys. Lett.*, 2016, **108**, 121103.
- 22 Q. Li, G. P. Liu, H. B. Yang, W. Wang, S. Luo, S. W. Dai and M. Qiu, *Appl. Phys. Lett.*, 2016, **108**, 193101.
- 23 D. Pan, H. Wei and H. X. Xu, *Chin. Phys. B*, 2013, **22**, 097305.
- 24 H. Wei, D. Pan and H. X. Xu, *Nanoscale*, 2015, **7**, 19053–19059.
- 25 Q. Li and M. Qiu, *Opt. Express*, 2013, **21**, 8587–8595.
- 26 H. Wei, Z. P. Li, X. R. Tian, Z. X. Wang, F. Z. Cong, N. Liu, S. P. Zhang, P. Nordlander, N. J. Halas and H. X. Xu, *Nano Lett.*, 2011, **11**, 471–475.
- 27 H. Wei, S. P. Zhang, X. R. Tian and H. X. Xu, *Proc. Natl. Acad. Sci. U. S. A.*, 2013, **110**, 4494–4499.
- 28 D. Pan, H. Wei, Z. L. Jia and H. X. Xu, *Sci. Rep.*, 2014, **4**, 4993.
- 29 Z. P. Li, K. Bao, Y. R. Fang, Y. Z. Huang, P. Nordlander and H. X. Xu, *Nano Lett.*, 2010, **10**, 1831–1835.
- 30 S. P. Zhang, H. Wei, K. Bao, U. Hakanson, N. J. Halas, P. Nordlander and H. X. Xu, *Phys. Rev. Lett.*, 2011, **107**, 096801.
- 31 Y. R. Fang, Z. P. Li, Y. Z. Huang, S. P. Zhang, P. Nordlander, N. J. Halas and H. X. Xu, *Nano Lett.*, 2010, **10**, 1950–1954.
- 32 Q. Hu, D. H. Xu, Y. Zhou, R. W. Peng, R. H. Fan, N. X. Fang, Q. J. Wang, X. R. Huang and M. Wang, *Sci. Rep.*, 2013, **3**, 3095.
- 33 Z. P. Li, S. P. Zhang, N. J. Halas, P. Nordlander and H. X. Xu, *Small*, 2011, **7**, 593–596.
- 34 H. Wei, Z. X. Wang, X. R. Tian, M. Kall and H. X. Xu, *Nat. Commun.*, 2011, **2**, 387.
- 35 H. Wei, X. R. Tian, D. Pan, L. Chen, Z. L. Jia and H. X. Xu, *Nano Lett.*, 2015, **15**, 560–564.
- 36 J. Grandidier, S. Massenet, G. C. des Francs, A. Bouhelier, J. C. Weeber, L. Markey, A. Dereux, J. Renger, M. U. Gonzalez and R. Quidant, *Phys. Rev. B*, 2008, **78**, 245419.
- 37 K. Hassan, A. Bouhelier, T. Bernardin, G. Colas-des-Francis, J. C. Weeber and A. Dereux, *Phys. Rev. B*, 2013, **87**, 195428.
- 38 T. Shegai, V. D. Miljkovic, K. Bao, H. X. Xu, P. Nordlander, P. Johansson and M. Kall, *Nano Lett.*, 2011, **11**, 706–711.
- 39 M. X. Song, A. Bouhelier, P. Bramant, J. Sharma, E. Dujardin, D. G. Zhang and G. Colas-des-Francis, *ACS Nano*, 2011, **5**, 5874–5880.
- 40 Z. X. Wang, H. Wei, D. Pan and H. X. Xu, *Laser Photonics Rev.*, 2014, **8**, 596–601.
- 41 H. B. Yang, M. Qiu and Q. Li, *Laser Photonics Rev.*, 2016, **10**, 278–286.
- 42 I. H. Malitson and M. J. Dodge, *J. Opt. Soc. Am.*, 1972, **62**, 1405.
- 43 P. B. Johnson and R. W. Christy, *Phys. Rev. B*, 1972, **6**, 4370–4379.
- 44 S. P. Zhang and H. X. Xu, *ACS Nano*, 2012, **6**, 8128–8135.